Progress In Electromagnetics Research, Vol. 143, 87–104, 2013

MICRO-DOPPLER ANALYSIS OF KOREAN OFFSHORE WIND TURBINE ON THE L-BAND RADAR

Joo-Ho Jung[1], Un Lee[2], Si-Ho Kim[3], and Sang-Hong Park[4,*]

[1]Department of Electrical Engineering, Pohang University of Science and Technology, Pohang, Gyungbuk, Korea

[2]Korea Southern Power Corporation, Seoul, Korea

[3]Agency for Defense Development, Daejeon, Korea

[4]Department of Electronic Engineering, Pukyong National University, Busan, Korea

Abstract—To cope with the energy shortage and the rising cost of the fossil fuel, many wind farms are being constructed under the supervision of Korean government along the coasts of Korean peninsula to generate clean and renewable energy. However, construction of these wind farms may cause negative effect on various L-band radars in operation. This paper presents the result of the micro-Doppler (MD) analysis of the influence of the wind turbine on the L-band radar using the point scatterer model and the radar cross section of the real turbine predicted by the method of physical optics. The simulation results obtained at three observation angles show that the range of MD occupies a considerable portion of the helicopter MD range, and thus, the operations using helicopters need to be avoided in the wind farm region, and additional radars are required for the recognition of helicopter-like objects.

1. INTRODUCTION

Nowadays many developed countries are focusing on the development of new renewable energy to cope with the soaring energy price and the pollution problems caused by the existing fossil fuel. Among several types of renewable energy, the wind power generation is the most well-established economical technique, and thus construction of the wind

Received 4 September 2013, Accepted 21 October 2013, Scheduled 28 October 2013

* Corresponding author: Sang-Hong Park (radar@pknu.ac.kr).

power plant is increasing. Following this global trend, many wind farms are being constructed by the Korean government onshore and offshore in Korean peninsula. Because many restrictions are imposed on the onshore wind farm owing to the difficulty in determining the location, noise of the wind turbine, the appearance of the wind farm, etc., most of the wind farms are being built offshore.

However, a great deal of controversy arose over the construction of the wind farm because of the L-band military radars installed along the coast of the Korean peninsula. These radars are surveying maritime and air targets for national security, and the wind turbines in the wind farm can interfere with the view of the radar. The major problem is the micro-Doppler (MD) effect caused by the rotating blade; the rotating blade in the stationary wind turbine causes additional MD frequency to the radar signal, and the reflected Doppler-modulated radar signal can be interpreted as a moving target, resulting in confusion in military operation as well as wasting military resources for identification. For these reasons, an in-depth MD analysis by the wind farm on the radar is an indispensable step for the successful supply of the energy while preserving the national security.

This paper examines the influence of wind turbine on the L-band radar constructed by the Korean representative wind turbine maker Samsung Heavy Industry (www.shi.samsung.co.kr). For accurate analysis, we considered the aspect angle of the radar toward the wind farm, design of the blade in the wind turbine, rotation and nutation of the blade. In the two sets of simulations using the blade composed of ideal point scatterers whose amplitudes were assigned empirically and predicted by the method of physical optics (PO), construction of the wind farm could give negative influence on the recognition of helicopters and the recognition of jet fighters could be possible because of the low MD frequency.

2. PRINCIPLES

2.1. Signal Modeling and Principle of Micro-Doppler

The monostatic chirp waveform [1] is assumed in this paper. The transmitted signal at fast-time t is given by

$$p(t) = A_0 e^{j2\pi(f_0 t + \frac{B}{2\tau}t^2)} \times \mathrm{rect}\left[\frac{t}{\tau}\right], \tag{1}$$

where A_0 is its amplitude, f_0 is the start frequency, B is the bandwidth, τ is the pulse duration and rect is a function whose value is 1 for $t - \tau/2 \leq t \leq t + \tau/2$ and 0 otherwise.

When a target is seen at various aspect angles, the radar observes it with an interval of pulse repetition period T_s. Thus we define a new slow-time variable by t_s given in T_s to express the variation of the radar signal for the entire observation time. Then, based on the geometric theory of diffraction [2], it is assumed that the target is composed of K scatterers and the received radar signal can be modeled by the sum of the chirp signals reflected from each scatterer as follows:

$$g(t,t_s)=\sum_{k=1}^{K}A_k e^{j2\pi\left(f_0(t-d_k(t_s))+\frac{B(t-d_k(t_k(t_s))^2}{2\tau}\right)}\times \mathrm{rect}\left[\frac{t-d_k(t_s)}{\tau}\right], \quad (2)$$

where A_k is the amplitude of scatterer k, and $d_k(t_s)$ is the fast-time delay between the radar and scatterer k at t_s. $d_k(t_s)=2r_k(t_s)/c$, in which c is the velocity light, is calculated assuming the plane wave, i.e., $r_k(t_s)$ is the distance of the scatterer k projected onto the radar line of sight (RLOS).

For higher resolution, the reflected signal is matched filtered by the following replica [3–7]:

$$s_o(t)=\exp\left(j2\pi\left[f_0t+0.5\frac{B}{\tau}t^2\right]\right)\times \mathrm{rect}\left(\frac{t}{\tau}\right), \quad (3)$$

and the resultant matched-filtered signal is given as follows [8]:

$$\begin{aligned} S_M(t,t_s) &= \sum_{k=1}^{K} IFT\{A_k\exp(-j2\pi f d_k(t_s))\} \\ &= \sum_{k=1}^{K} A_k \mathrm{sinc}(B(t-d_k(t_s))). \end{aligned} \quad (4)$$

In the range domain, (4) can be expressed by

$$S_M(r,t_s)=\sum_{k=1}^{K}A_k\mathrm{sinc}(B(r-d_k(t_s))), \quad (5)$$

where $r=ct/2$. Note that (5) is a set of range profiles collected for various t_s values. Therefore, MD is caused by the time-varying $d_k(t_s)$, and using the well-known Doppler formula [9], the following MD for each r is generated at t_s from the scatterer k:

$$\mathrm{MD}_k(t_s)=-\frac{2v_{los}}{\lambda}=-\frac{2}{\lambda}\frac{dd_k(t_s)}{dt_s}\bigg|_{los}, \quad (6)$$

where v represents the velocity of the target, and the subscript *los* represents projection onto the radar line-of-sight.

Based on (6), MD for each r can be represented by performing the Fourier transform (FT) of the radar signal in t_s. However, because the micro-motion of the target changes significantly for t_s, MD changes accordingly. Therefore, it is more profitable to express MD in the time-frequency domain. In this paper we apply the short-time FT (STFT), which is a method sequentially expressing FT of the clipped signal $s(t_s)$ around t_s as follows (Fig. 1) [10, 11]:

$$STFT(t_s, f_s) = \int s(t')w(t' - t_s)\exp(-j2\pi f_s t')dt', \tag{7}$$

where $w(t_s)$ is a window function used to remove the high sidelobes around the peak in frequency domain and f_s the slow-time frequency.

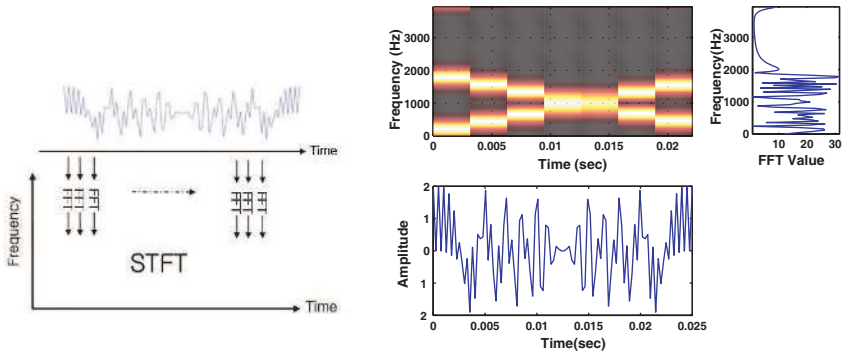

(a) (b)

Figure 1. Principle and example of STFT. (a) Principle of STFT. (b) Example of STFT.

2.2. Modeling of Blade Motion in Wind Turbine

In this paper, we assume that the motion of the blade in the wind turbine is composed of two components; spinning and nutation (Fig. 2). Spinning is the rotation of blades around a spinning axis and nutation is the rotation of the target by a sinusoidal angle in the plane formed by the spinning axis and the blade axis. Contrary to the fixed spinning axis, the nutation plane changes because of the time-varying axis of each blade.

Spinning can be easily explained by the Rodrigues rotation formula which represents the spinning motion using a simple rotation matrix. Assuming that a scatterer located at a position vector $\vec{p_0}$ rotates around a spinning axis $\vec{a} = [a_x\ a_y\ a_z]$ with an angular velocity

ω_s, the position of the scatterer at t_s is expressed by the following matrix formula [12]:

$$\vec{p_s} = (\mathbf{I}\cos\omega_s t_s + [\vec{\alpha}]_x \sin\omega_s t_s + (1-\cos\omega_s t_s)\,\vec{\alpha}\vec{\alpha}^T = \mathbf{R}_s\vec{p}_0, \tag{8}$$

where $\mathbf{I}$ is the 3×3 identity matrix, and the superscript T is the vector transposition. The cross product matrix $[\vec{\alpha}_x]$ is given by

$$[\vec{\alpha}]_x = \begin{bmatrix} 0 & -\alpha_z & \alpha_y \\ \alpha_y & 0 & -\alpha_x \\ -\alpha_y & \alpha_x & 0 \end{bmatrix}. \tag{9}$$

Nutation can be modeled by three steps: transformation of the vector located in (x, y, z) coordinate into that in a new coordinate in (x', y', z') formed by the spinning and the blade axes, rotation of the transformed vector by the sinusoidally varying angle $\theta(t_s) = \theta_0 \sin(\omega_n t_s)$, where θ_0 is the amplitude and ω_n is the angular velocity of nutation, and transformation of the rotated vector into the (x, y, z) coordinate (Fig. 3) [13].

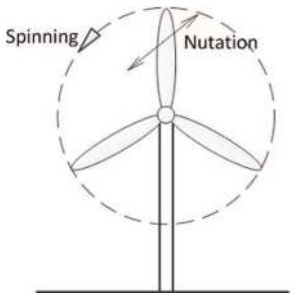

Figure 2. Motion of the blade.

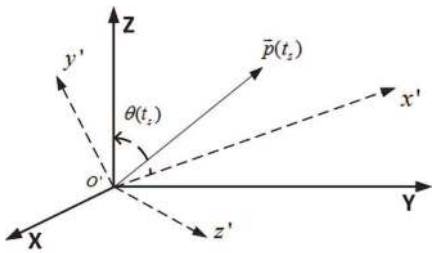

Figure 3. New coordinate for nutation [13].

To derive the transformation matrix, the relationship between the unit vectors in (x, y, z) and that in (x', y', z') is required. With the normalized spinning axis being the unit vector $\hat{x}$ in x' axis, unit vector $\hat{z}$ in z' axis is derived by normalizing the cross product between $\vec{p}(t_s)$ and the real-time blade axis. In the same manner, $\hat{y}$ is generated by normalizing the cross product between $\hat{z}$ and $\hat{x}$. Then, the transformation matrix $\mathbf{T}$ into (x', y', z') is given as follows [13]:

$$\mathbf{T}(t_s) = [\hat{x}\ \hat{y}\ \hat{z}], \tag{10}$$

and (8) is transformed into (x', y', z') as follows:

$$\vec{p'}(t_s) = \mathbf{T}^T(t_s)\vec{p}(t_s). \tag{11}$$

Then, $\vec{p'}(t_s)$ is rotated in x'-y' plane using the following rotation matrix operation:

$$\vec{p'}_{rot}(t_s) = \mathbf{R}_{rot}\vec{p'}(t_s), \tag{12}$$

where the matrix $\mathbf{R}_{rot}(t_s)$ is given by

$$\mathbf{R}_{rot}(t_s) = \begin{bmatrix} \cos\theta(t_s) & -\sin\theta(t_s) & 0 \\ \sin\theta(t_s) & \cos\theta(t_s) & 0 \\ 0 & 0 & 1 \end{bmatrix}. \tag{13}$$

Finally, (12) is transformed back into (x, y, z) as follows (see [13] for the detailed procedure):

$$\vec{p}_{nut}(t_s) = \mathbf{T}(t_s)\vec{p'}_{rot}(t_s). \tag{14}$$

2.3. Method of Extracting the Scatterers

In this paper, we extracted the complex amplitude of the scatterer in the blade, which is A_k in (2). For this purpose, we divided each blade into five segments and measured the radar cross section (RCS) of each segment (Fig. 4). Because RCS of a blade-like rode can be assumed to be a single scatterer [3], division into five segments can provide more accurate RCS prediction.

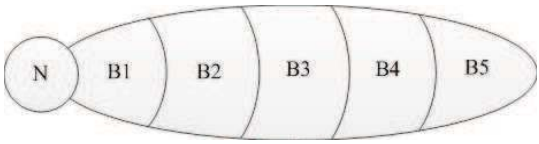

Figure 4. Five segments of a blade; one segment was used for the nacelle (N) and five segments for the blade (B1–B5).

In predicting the RCS of the segment, the method of physical optics (PO) that computes the specular return of the transmitted radar signal was used [14]. Assuming that the target is much larger than the wavelength and plane wave, PO represents the reflected radar signal that uses a sum of the signal from the polygons, normally triangles and rectangles, that comprise the target. When a facet with an area F_p is observed in the direction of z-axis, the vertical and horizontal components of the scattered electric field given as follows [14]:

$$\begin{bmatrix} E_{sh} \\ E_{sv} \end{bmatrix} = -\frac{jke^{jkr}}{2\pi}\int_{F_p} e^{2jkz'}dx'dy' \times \begin{bmatrix} R_G n_x^2 - R_E n_y^2 & (R_H + R_E)n_x n_y \\ (R_H + R_E)n_x n_y & R_G n_y^2 - R_E n_x^2 \end{bmatrix} \begin{bmatrix} E_{ih} \\ E_{iv} \end{bmatrix}, \tag{15}$$

where n_x, n_y and n_z are the x, y and z components of the unit normal vector of the facet. R_H and R_E are the reflection coefficients of H and E polarizations. The analytic solution of the phase integral in (15) provides fast calculation (see [15] for the details).

2.4. Analysis Procedure

Figure 5 summarizes the analysis procedure. The blade motion was modeled using (8)–(14), and the radar signal was constructed using (4) for various pulses (slow-time t_s). Then, matched filtering was conducted for each t_s using (5), and the range bin with the maximum energy was selected; for each range bin, the energy was defined to be the sum of the absolute values of the squared signal for all t_s. Finally, STFT of the selected range bin was conducted and the MD was analyzed in time-frequency domain. In analyzing MD of the blade, Table 1 was used as a reference assuming the center frequency = 1.2 GHz.

Table 1. Velocities of aircraft and corresponding Doppler frequency (center frequency = 1.2 GHz).

Aircraft	**Velocity**	**Maximum Doppler frequency**
Mig-25	926.8 m/s	7.41 kHz
Mig-31	926.8 m/s	7.41 kHz
Su-27	777.85 m/s	6.22 kHz
Mig-23	777.85 m/s	6.22 kHz
F-4	761.3 m/s	6.09 kHz
F-15	827.5 m/s	6.62 kHz
T-50	496.5 m/s	3.97 kHz
Passenger airplane	222–277 m/s	1.78–2.22 kHz
Helicopter (Apache)	81.39 m/s	0.651 kHz
Transport plane	258.333 m/s	2.07 kHz

3. SIMULATION RESULTS

3.1. Simulation Condition

In simulations we used a model composed of three blades (Fig. 6(a)); each blade was composed of five isotropic point scatterers, and one scatterer was generated for the nacelle at the model center. To be

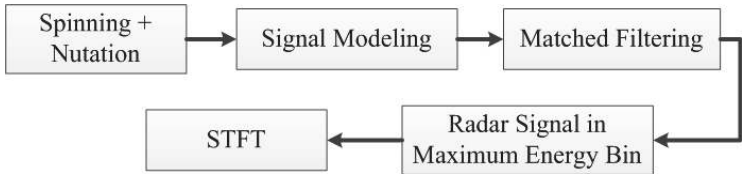

Figure 5. Analysis procedure.

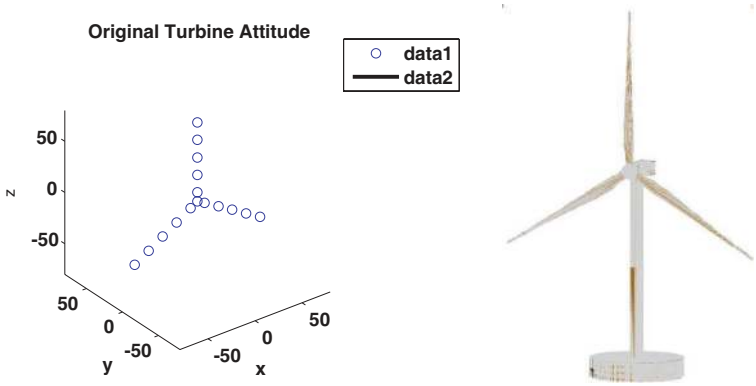

Figure 6. Scatterer model and the real CAD model. (a) Scatterer model. (b) CAD model.

realistic, the position of the scatterer was determined using the three-dimensional CAD data of the real wind turbine developed by Heavy Industry (Fig. 6(b)), and the amplitude of each scatterer in Fig. 4 was assigned to reflect the scattering mechanism; N = 10, B1 = 5, B2 = 8, B3 = 5, B4 = 3, B5 = 1. For the radar system, we used a monostatic chirp radar with pulse repetition frequency = 2 kHz, center frequency = 1.2 GHz, B = 1.6 MHz and $\tau = 30\,\mu$s.

Observation was conducted for the blade model located at 10 Km from the radar at three different aspect angles, 0° 45° and 90° (Fig. 7). For each observation angle, a fast rotation with the rotation per minute (RPM) = 10.2 was simulated on the basis of motion parameters measured and analyzed in various coasts of Korean peninsula by Samsung Heavy Industry. For nutation, $\omega_n = 3\pi$ was used with $\theta_0 = 1°$ to simulate the fast nutation. Table 2 summarizes the parameters used for simulation.

Table 2. Parameters used for simulation.

Center frequency	1.2 GHz	Aspect angle	$0°, 45°, 90°$
Bandwidth	1.6 MHz	No. of total scatterers	16
Pulse width	30 μs	RPM	10.2
Distance to the blade	10 Km	Nutation ($\theta_0 = 1°$)	$\theta_n = 3\pi$ rad/s

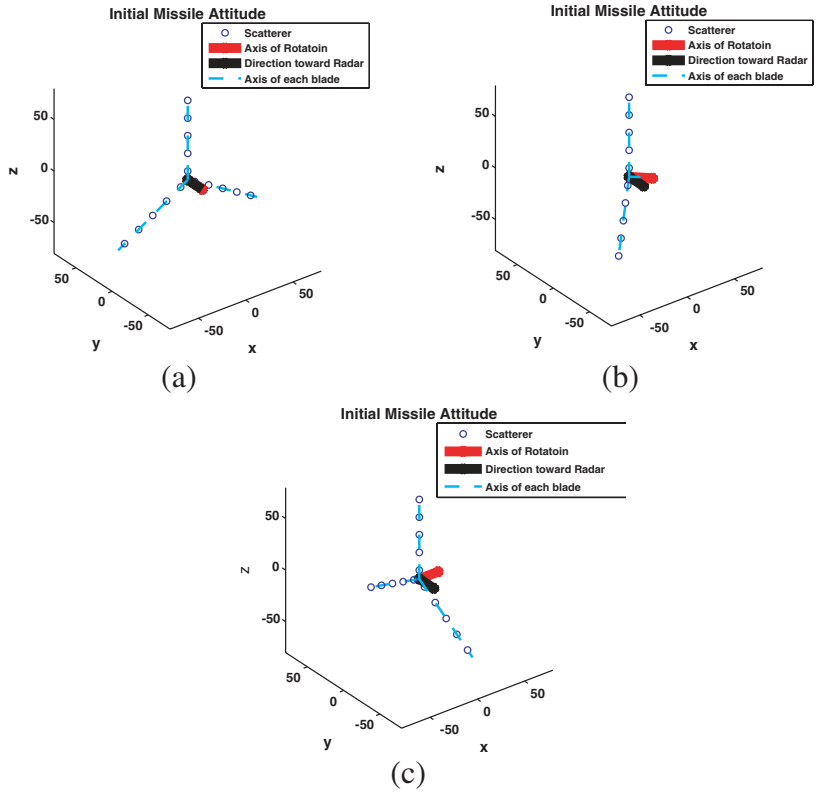

Figure 7. Geometry of radar observation. (a) 0°. (b) 45°. (c) 90°.

3.2. Simulation Results Using Ideal Point Scatterers

Each scatterer has equal time delay at 0° aspect angle in the absence of nutation because of the equal distance projected onto RLOS. Thus, the range profiles measured using different pulses (= cross-range bins)

are invariant while those at 45° and 90° vary significantly due to the time-varying distance of the scatterer (Fig. 8). STFT was applied to the range bin with the maximum energy specified by the rectangle to analyze the MD. Because of the invariant range profiles at 0° aspect angle, the signals specified in Fig. 8(a) had the identical amplitude and phase. Therefore, following the principle in (6), MD measured at 0° yielded zero Doppler only (Fig. 9(a)). However, because of the time-varying nature of the signal at 45° and 90°, time-varying sinusoidal MD images were generated (Figs. 9(b) and (c)).

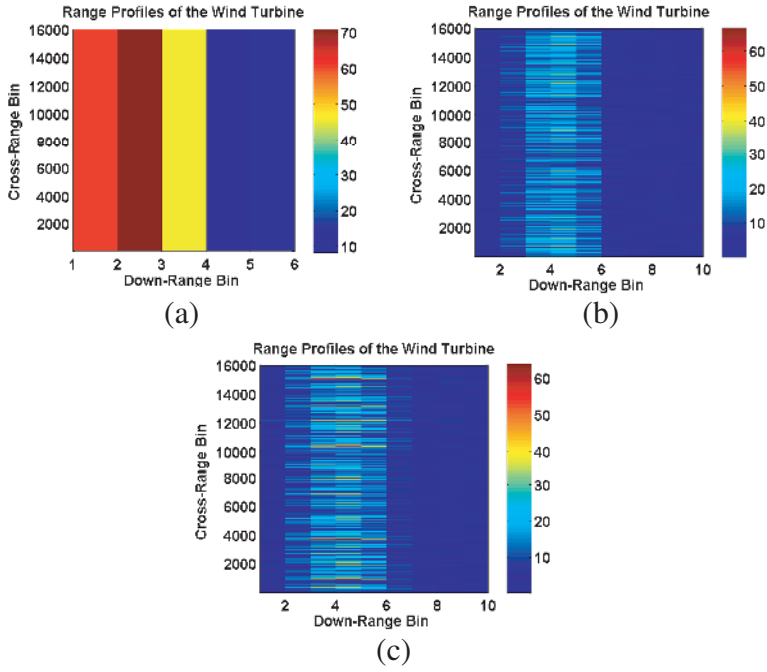

Figure 8. Range profiles for three aspect angles (without nutation). (a) 0°. (b) 45°. (c) 90°.

The MD image of the blade provides the information on the blade type and the blade motion in Figs. 9(b) and (c). Corresponding to 16 scatterers, 16 lines appeared in the MD image; one zero Doppler line was generated because of the nacelle fixed at the scene center, and 15 sinusoidal Doppler curves representing 15 scatterers were generated. Because the velocity of the scatterer and the resulting Doppler frequency increased in proportion to the distance from the center, each sinusoidal curve had a different amplitude. In addition,

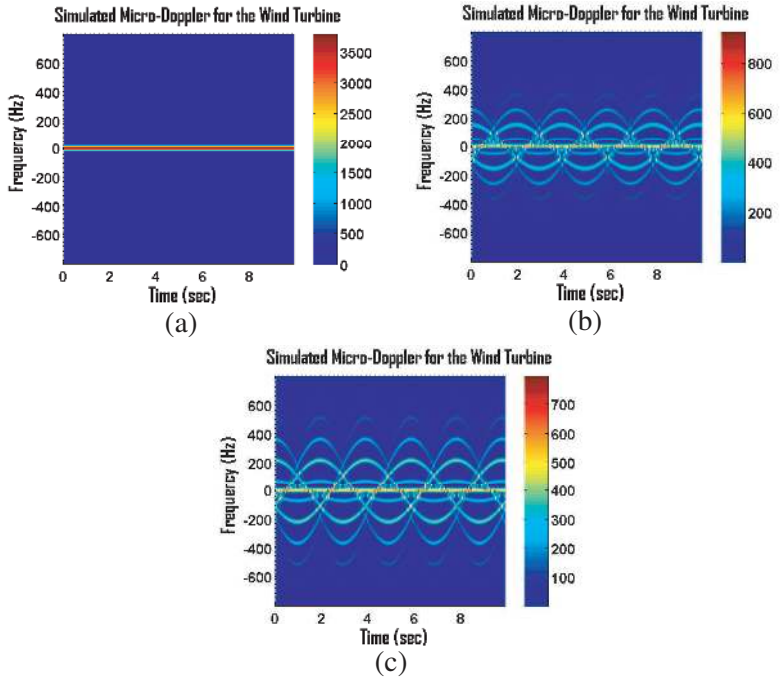

Figure 9. Micro-Doppler results for three aspect angles (without nutation). (a) 0°. (b) 45°. (c) 90°.

the value of the sinusoidal curve differed depending on the RCS value assigned to each scatterer; three B2s were clearly seen due to the largest RCS value, and three B5s dimly appeared due to the smallest RCS.

The period of the sinusoidal curve provides the rotational velocity; the sinusoidal curve repeated with the period $T_s = 5.88\,\text{s}$ and the angular velocity $\omega_s = 1.07\,\text{rad/s}$, which is equal to the angular velocity corresponding to the RPM = 10.2. Comparing the range of the Doppler frequency, MD for 45° ranged between −500 and 500 Hz and that for 90° was between −700 and 70 Hz. This range includes the entire range of the Doppler frequency by the helicopter (−651–651 Hz in Table 1). However, considering the fact that the general aspect angle of the blade is smaller than 60° and that 90° is the condition for maximum Doppler, the helicopter could be partially screened by the wind turbine.

When compared with the zero-Doppler obtained at 0° aspect angle without nutation, the forward-backward nutation caused time-varying MD (Fig. 10(a)); the periodic MD appeared with a period and an amplitude equal to 0.67 s and 80 Hz, respectively. As illustrated

in Table 1, the helicopter could be partially blocked by the wind turbine. At 45° aspect angle, the nutation fluctuated the sinusoidal MD (Fig. 10(b)), obscuring the period and the amplitude of the sinusoidal curves. The Doppler ranges approximately between −500 and 500 Hz, which can interfere with the indication of the helicopter. At 90° observation angle, the nutation did not influence the MD signature because of the perpendicularity between the direction of nutation and RLOS (Figs. 8(c) and 9(c)). Thus the analytical results of the three aspect angles and the general aspect angle indicate that the wind turbine interferes with the radar operation to indicate the helicopter-like object.

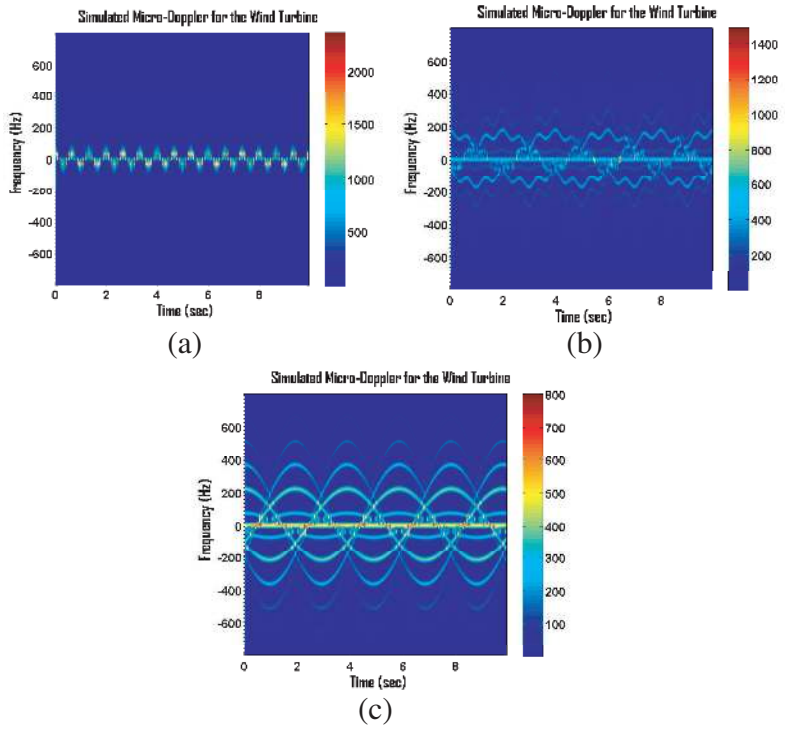

Figure 10. Micro-Doppler results for three aspect angles (with nutation). (a) 0°. (b) 45°. (c) 90°.

3.3. Simulation Results Obtained from Predicted Scatterers

To be more realistic, the blade was divided into five segments (B1–B5) (Fig. 11), the RCS of the blade segments was predicted for each

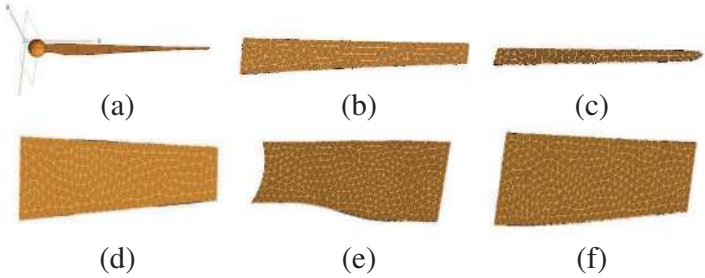

Figure 11. Blade model and five segments. (a) Blade. (b) B1. (c) B2. (d) B3. (e) B4. (f) B5.

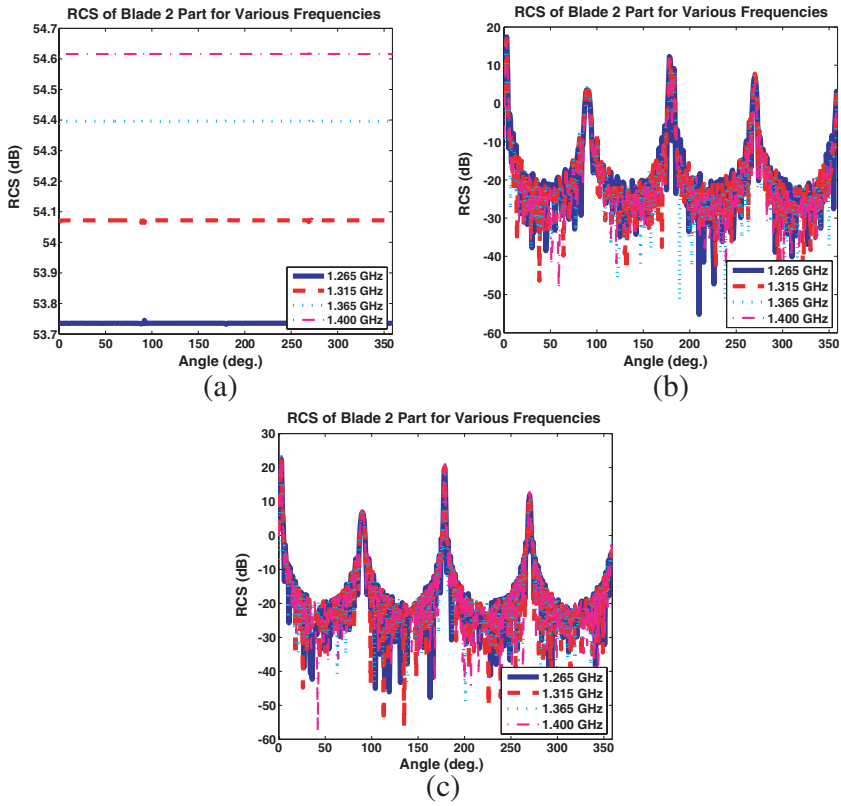

Figure 12. RCS variation versus rotation angle at three aspect angles. (a) 0°. (b) 45°. (c) 90°.

segment using PO, and the predicted complex RCS was applied to A_k in (2). The sphere-shaped nacelle was also regarded as a scatterer and the omnidirectional RCS was input to (2). At 0° aspect angle, the RCS of the segment 2 (B2) derived for the major four center frequencies in L-band was stable for all rotation angles because the relative aspect between the radar and B2 did not vary. However, at 45° and 90°, the RCS of the segment 2 (B2) varied significantly depending on the azimuth angle (Fig. 12). The other four yielded similar patterns and thus were omitted.

In contrast to that shown in Fig. 9, the MD image was significantly different except for 0° because of the RCS variation (Fig. 13(a)). Owing to the perpendicularity between the radar line of sight and the direction of rotation, variation of RCS did not affect MD at 0°. Thus, zero-Doppler was generated for the entire observation time. However, RCS dropped significantly even though the scatterer was rotated by a small

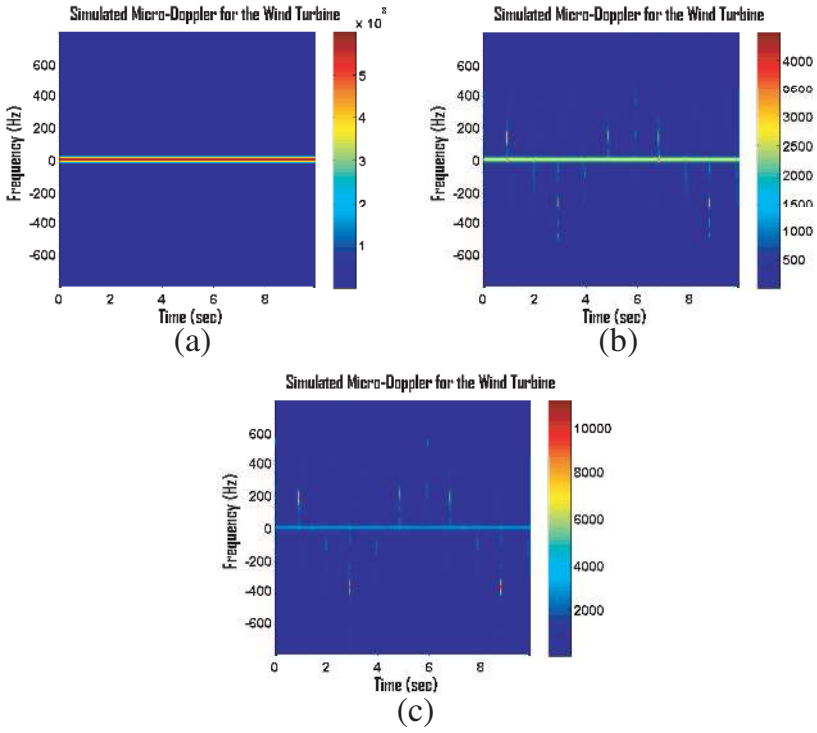

Figure 13. Micro-Doppler results using the real RCS for three aspect angles (without nutation). (a) 0°. (b) 45°. (c) 90°.

angle from that of peak (see Figs. 13(b) and (c)). As a result, contrary to the sinusoidal curves observed for the entire rotation time (Fig. 9), blade flashes were seen when the blade arrived at the angle of the peak RCS.

Though the MD signature was different from that derived by using the isotropic point scatterer, the information on the blade movement derived from the MD image was identical. The peak appearing at 0 s appeared again at 5.88 s corresponding to the $T_s = 5.88$ s, $\omega_s = 1.07$ rad/s and RPM = 10.2 (Figs. 13(b) and (c)). The range of MD for 45° was between −500 and 500 Hz, and that for 90° was between −700 and 700 Hz. Thus, as in the simulation using isotropic point scatterer, the helicopter could be partially screened by the wind turbine

As shown in Fig. 10(a), the nutation caused time-varying MD at 0° aspect angle (Fig. 14(a)); periodic MD appeared with a period

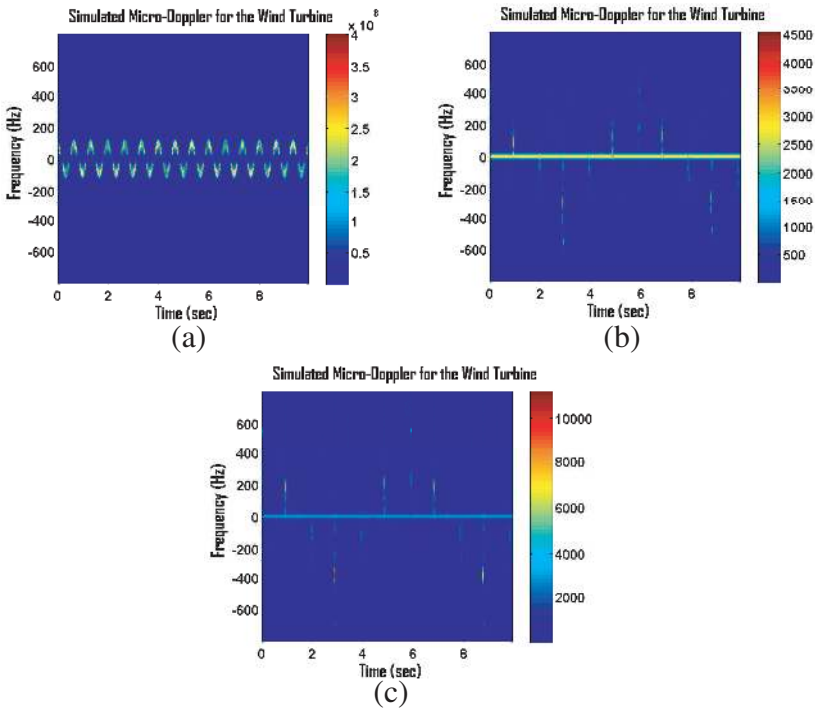

Figure 14. Micro-Doppler results for three aspect angles (with nutation). (a) 0°. (b) 45°. (c) 90°.

and an amplitude equal to 0.67 s and 80 Hz, respectively. Thus, the helicopter could be partially blocked by the wind turbine (see Table 1). At 45° aspect angle, nutation did not affect the blade flash except for a small amount of spread (Fig. 14(b)). The blade flash ranged approximately between −500 and 440 Hz, which is within the helicopter MD. At 90° observation angle, no effect of nutation was found because of the perpendicularity between the direction of nutation and RLOS (Fig. 14(c)). Therefore, as in the analysis using the ideal point scatterers, we concluded that the wind turbine interferes with the radar operation to indicate the helicopter-like object.

4. CONCLUSION

In this paper, we analyzed the effect of MD in the Korean wind turbine on the indication of moving target by the L-band radar. For this study we used the real wind turbine model constructed by the Korean representative wind turbine maker Samsung Heavy Industry. In both simulations using ideal point scatterers and RCS of the real wind turbine model predicted by PO, the range of MD was within the Doppler range generated by the helicopter, and recognition of target could be seriously interrupted when the target coincided with the blade flash with the large RCS. Therefore, military operations that use helicopters should be avoided. For successful recognition of the target flying near the wind farm, other types of radars such as imaging and high-resolution radars are required. Nutation of the blade caused MD even though RLOS and the direction of rotation were perpendicular at 0° observation; however, the range of MD was very small and within the range of helicopter MD. For 45° observation, nutation did not change the overall range of MD significantly, giving little influence to the MD result.

Based on the procedure established in this paper, various wind farms presently under construction in Korea will be analyzed, and the result will be provided to the Ministry of National Defense as a reference for military operations that use the L-band radar. Furthermore, many other types of radars are in operation along the Korean peninsula, and construction of wind farms may also affect these radars. Currently, we are analyzing the effect of the wind farm on the track-while-scan radar that uses the wind turbine constructed by SK Construction which is another Korean major manufacturer of wind turbines. A more advanced method will be developed based on the procedure proposed in this paper, and the analysis result will be published soon in open literature.

ACKNOWLEDGMENT

This research was supported by Basic Science Research Program through the National Research Foundation of Korea(NRF) funded by the Ministry of Education, Science and Technology (2012R1A1A1002047). This work was supported by the STRL (Sensor Target Recognition Laboratory) program of Defense Acquisition Program Administration and Agency for Defense Development.

REFERENCES

1. Park, S.-H., M.-G. Joo, and K.-T. Kim, "Construction of ISAR training database for automatic target recognition," *Journal of Electromagnetic Waves and Applications*, Vol. 25, Nos. 11–12, 1493–1503, 2011.
2. Potter, L. C., D. M. Chiang, R. Carriere, and M. J. Gerry, "A GTD-based parametric model for radar scattering," *IEEE Transations on Antennas and Propagation*, Vol. 43, No. 10, 1058–1067, Oct. 1995.
3. Mahafza, B. R., *Radar Systems Analysis and Design Using MATLAB*, Chapman & Hall/CRC, 2000.
4. Jung, J.-H and S.-H. Park, "Efficient classification of low-resolution range profiles of automobiles using a combination of useful features," *Progress In Electromagnetics Research*, Vol. 139, 373–387, 2013.
5. Park, S.-H., "Automatic recognition of targets in formation using range profiles," *Journal of Electromagnetic Waves and Applications*, Vol. 26, Nos. 14–15, 2059–2069, 2012.
6. Park, S.-H., J.-I. Park, and K.-T. Kim, "Motion Compensation for squint mode spotlight SAR imaging using efficient 2D interpolation," *Progress In Electromagnetics Research*, Vol. 128, 503–518, 2012.
7. Park, S.-H., J.-H. Lee, and K.-T. Kim, "Performance analysis of the scenario-based construction method for real target ISAR recognition," *Progress In Electromagnetics Research*, Vol. 128, 137–151, 2012.
8. Cumming, I. G. and F. H. Wong, *Digital Processing of Synthetic Aperture Radar Data*, Artech House, 2005.
9. Skolnik, M., *Introduction to Radar Systems*, McGRAW-Hill, 2001.
10. Qian, S., *Introduction to Time-frequency and Wavelet Transforms*, Prentice Hall, 2001.

11. Qian, S. and D. Chen, *Joint Time-frequency Analysis*, Prentice Hall, 1998.
12. Chen, V. C., *The Micro-Doppler Effect in Radar*, Artech House, 2011.
13. Gao, H., L. Xie, S. Wen and Y. Kuang, "Micro-Doppler signature extraction from ballistic target with micro-motions," *IEEE Transactions on Aerospace and Electronic Systems*, Vol. 46, No. 4, 1969–1982, Oct. 2010.
14. Park, S.-H., K.-K. Park, J.-H. Jung, H.-T. Kim, and K.-T. Kim, "Construction of training database based on high frequency RCS prediction method for ATR," *Journal of Electromagnetic Waves and Applications*, Vol. 22, Nos. 5–6, 693–703, 2008.
15. Klement, D., J. Preissner, and V. Stein, "Special problems in applying the physical optics method for backscatter computations of complicated objects," *IEEE Transactions on Antennas and Propagation*, Vol. 36, No. 2, 228–237, Feb. 1988.